Oral presentation | Fluid-structure interaction
Fluid-structure interaction-I
Mon. Jul 15, 2024 10:45 AM - 12:45 PM Room A

[1-A-01] Effect of Pitch-Sweep Overlap on Lift in Clap-and-Peel Motion

*Farhanuddin Ahmed[1], Nipun Arora[1] (1. Indian Institute of Technology, Jodhpur)

Keywords: Clap-and-peel, Lattice Boltzmann method, Insect Aerodynamics

**Twelfth International Conference on
Computational Fluid Dynamics (ICCFD12),
Kobe, Japan, July 14-19, 2024**

Effect of Pitch-Sweep Overlap on Lift in Clap-and-Peel Motion

F. Ahmed and N. Arora*
*Corresponding author: nipun@iitj.ac.in
Indian Institute of Technology Jodhpur, Rajasthan, India.

Abstract: The study aims to examine various aerodynamic phenomena and flow configurations that elucidate the principles of lift generation in minuscule insects. Simulations are conducted on three-dimensional wings that execute a "clap-and-peel" motion, inspired by the flying of *Drosophila melanogaster*. A numerical fluid solver is created using the multiple relaxation time (MRT) model of the lattice Boltzmann method (LBM). A dynamic mesh refinement technique was employed to enhance the resolution of the grid region encompassing the mobile geometry. Validations were performed to verify the applicability of LBM for deforming borders. The tests involved flapping rectangular wings with time-varying changes in chordwise camber and twist. The study investigates the impact of the pitching-sweeping overlap ξ, ranging from 0% to 100%, on the characteristics of lift and drag. At $\xi = 100\%$, the mean lift is approximately 36.4% higher compared to when $\xi = 0\%$ at a Reynolds number of 200. This significant increase is related to the formation of a strong leading edge vortex (LEV) during the clap phase in the former case. The aerodynamics of the clap-and-peel mechanism were compared to a single-wing flapping, resulting in a 31.7% increase in the average lift coefficient.

Keywords: Lattice Boltzmann Method, Insect aerodynamics, Clap-and-Peel, Overlap.

1 INTRODUCTION

Flapping-wing aerodynamics has captured the attention of researchers, driven by the escalating design initiatives in the domain of Micro Aerial Vehicles (MAVs). These compact unmanned air vehicles are characterized by dimensions not exceeding 15 cm [1]. Advancements in various technological domains have paved the way for utilizing MAVs as agile and discreet sensing platforms capable of gathering intelligence in hazardous and physically inaccessible areas. To successfully execute such missions, MAVs need to exhibit effortless manoeuvrability, sustained flight, and efficient propulsion. However, traditional methods of generating thrust and lift prove inefficient in meeting the required capabilities at these scales, leading to the essential adoption of flapping-wing propulsion [2]. Flapping wing Micro Air Vehicles (FWMAVs) demonstrate enhanced efficiency, especially in areas that requires hovering conditions and a compact size. However, downsizing introduces aerodynamic and flight control challenges. Numerous research efforts have been undertaken to comprehend the aerodynamic principles around flapping wings through both numerical simulations and experimental approaches.

Previously, researchers have primarily focused on the flapping movement of rigid wings and examined flexibility mainly in two dimensions for the wings of small insects [3, 4, 5]. Flexibility has been observed to transform the fling phase of clap-and-fling motion into a motion that resembles a peel, while the clap phase can be compared to a reverse-peel [6]. In the fling phase, flexible wings enhance lift by enhancing circulation, and in the clap phase, they enhance the downward momentum flow [7]. Miller and Peskin [3] computationally investigated this phenomenon in two dimensions at Re=10. Their results indicate that clap-and-fling with flexible wings generates a higher lift and less drag than clap-and-fling with rigid wings. Tian et al. [4] numerically investigated the effect of flexible wing sections on the generation of forces during forward flight. They noticed that the wing's dynamic pitching can significantly enhance both thrust and thrust-to-power ratio while also maintaining or increasing lift and lift-to-power ratio at the same time. Percin et al. [5] experimentally investigated the clap-and-peel motion on Delfly wings and observed that during the peeling phase, the vortex pairs generated induce a strong inflow, forming a low-pressure region between upper and lower wings. This, along with leading-edge vortices and increased momentum from the clap, formed a higher force during the downstroke. Jankauski et al. [8] found that the presence of flexibility in wings decreases power by 25% when compared to wings that are rigid. Lehmann et al. [9] discovered an unconventional energy recuperation mechanism in an insect that recaptures the rotational energy of vortices and transfers this kinetic energy to the wing instantly. They observed a

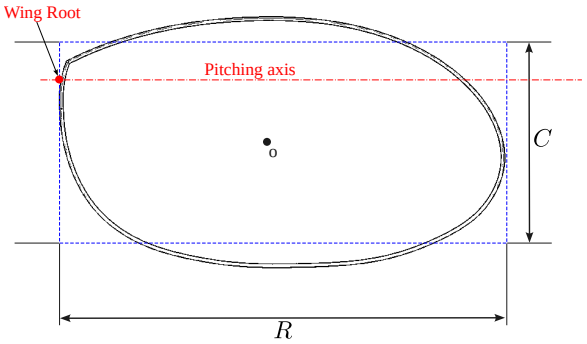

Figure 1: A schematic of wing planform of *fruit fly* [18] illustrating important geometry parameters: wing span R, mean chord C and the axis of wing rotation during pitching.

reduction in flight power requirement by utilizing kinetic energy from the motion of the surrounding air through chordwise wing bending.

The temporal variation of wing deformation over time was initially outlined by Ellington [6] and Ennos [10] through their qualitative analysis of hovering insects captured on a single high-speed camera. Recently, Walker et al. [11] obtained qualitative data using four high-speed digital cameras to observe free-flying droneflies. Du and Sun [12] numerically investigated the effect of camber and twist as recorded by Walker and observed an increase in lift coefficient by 10% to 20% as compared to the rigid wing. It was hypothesised that the camber and twist initially rose from zero to a specific constant value, remained constant in the middle portion of the half-stroke, and then began to decline in the later part of the half-stroke, ultimately reaching zero at the end.

In the present study, we build upon our previous work on clap-and-fling [13] and extend it to deforming wings with more realistic kinematics using an in-house fluid solver based on the multi-relaxation time (MRT) lattice Boltzmann method (LBM) [14, 15]. The objective of our study is to analyse how the timing of pitching and sweeping, measured by the parameter ξ, affect the average lift and drag coefficients, denoted as $< C_L >$ and $< C_D >$, respectively. This study aims to enhance our comprehension of the diverse flow structures linked to the "clap-and-peel" motion and its influence on lift production. This knowledge will assist in the advancement of next-generation bio-inspired Micro Air Vehicles (MAVs). Hence, the primary objectives of this investigation are:

(a) Development of a three-dimensional in-house numerical solver based on the MRT-LBM to analyze various aerodynamic phenomena and flow structures, elucidating the dynamics of force generation by deforming wings using the "clap-and-peel" mechanism.

(b) Perform a parametric study to quantify the dependence of average lift and drag by varying degrees of overlap between pitching and sweeping (ξ).

(c) Identify the optimum “clap-and-peel" operating conditions with respect to lift to drag ratio.

2 PROBLEM DESCRIPTION

A model wing based on the planform of *Drosophila melanogaster* (fruit fly) has been recreated from [16] using image processing tools [17]. The section thickness of the wing model is 1.5% of the mean chord length with rounded leading and trailing edges. The wing has a span (R) of 2.16 mm and a mean chord (C) of 0.77 mm. An idealised wing kinematics for three-dimensional clap-and-peel motion is proposed based on the experimental data of Miller and Peskin [3]. The wing's flight cycle begins with the fling phase, during which it rotates around its trailing edge. As the wings fling apart, they are deformed along the chord, creating a peel effect. Following this, the wings perform the downstroke with a positive camber by rotating around its root, during which the angle of attack varies from root to tip, obtaining a higher angle of attack at the tip. Towards the end of the downstroke, the wing flips around its rotation axis, obtaining a positive angle of attack while sweeping in the reverse direction, marking the start of the upstroke. During this phase, the wings reverses its deformation to maintain a positive camber. Upon completing the upstroke, the wing returns to its original position and straightens while rotating about the leading edge to complete the clap phase.

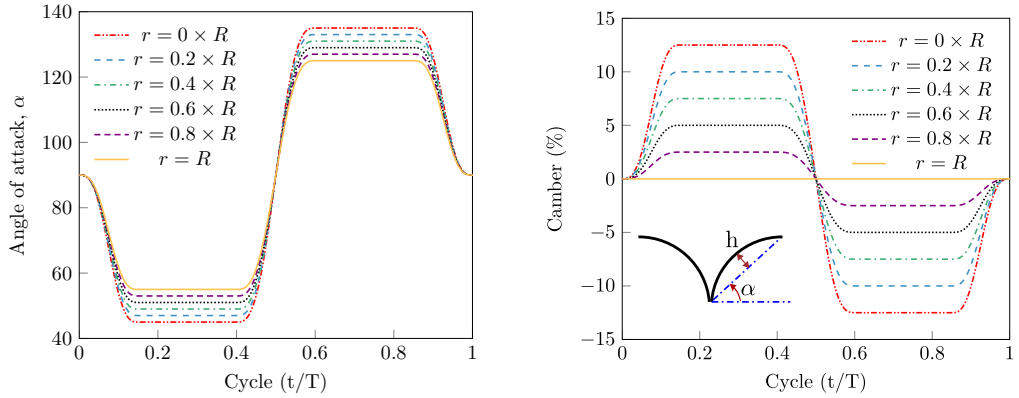

(a) (b)

Figure 2: Time history of (a) pitching angle and (b) percentage camber at different wing sections over one stroke cycle.

Table 1: Details of kinematics parameters used in the numerical simulation.

Parameter	Value
$\alpha^*_{m,root}$	45°
$\alpha^*_{m,tip}$	35°
ϕ_0	0°
ϕ_m	65°
$h_{m,root}$	$0 \times C$
$h_{m,tip}$	$0.125 \times C$

2.1 Kinematic modelling

The wing movements were estimated with certain approximations to simulate the dynamic morphing of an actual fruit fly wing. The wing pair is positioned with a gap equal to 7.5% of the average chord length. A linear relationship was assumed between the Euler angle in the spanwise direction, radius (r), and time (τ). The time-dependent stroke angles were considered uniform across all wing cross-sections, as shown in Fig. 2. The pitching and sweeping velocities are given as,

$$\dot{\alpha}(r,\tau) = \frac{\alpha^*_m(r)}{\Delta\tau^*}\left(1 - \cos\left[2\pi\left(\tau - \tau^*\right)/\Delta\tau^*\right]\right) \tag{1}$$

$$\dot{\phi}(\tau) = \frac{\phi_m}{\Delta\tau^*}\left(1 - \cos\left[2\pi\left(\tau - \tau^*\right)/\Delta\tau^*\right]\right) \tag{2}$$

where $\alpha_m(r)$ and ϕ_m is the maximum angular amplitude at any wing length r. The time sequence of a cycle is governed by their starting time τ^* and time duration $\Delta\tau^*$ for different phases. The amplitude of the angle of attack over the length of the wing varies linearly according to the following equation:

$$\alpha^*_m(r) = \alpha^*_{m,root} + (\alpha^*_{m,root} - \alpha^*_{m,tip})\frac{r}{R} \tag{3}$$

where $\alpha^*_{m,root}$ and $\alpha^*_{m,tip}$ are the amplitude of attack angle at root and tip, respectively. Figure. 2a illustrates the time-dependent variation in the pitching angle across different wing sections. The twist is assumed to be linear and can, therefore, be determined by the twist angle, which is the difference in the geometrical angle of attack between the wing tip ($\alpha^*_{m,tip}$) and the wing root ($\alpha^*_{m,root}$).

The equation of the mean lines of the NACA four-digit wing sections is used for the modelling of the camber in the wing cross sections [12], as

$$h(r,x,\tau) = \begin{cases} \frac{h_m(r,\tau)}{p^2}(2px - x^2), & (0 \le x \le p) \\ \frac{h_m(r,\tau)}{(1-p)^2}((1-2p) + 2px - x^2), & (p < x \le 1) \end{cases} \tag{4}$$

where x is the chordwise position normalized by the local chord length $c(r)$, $h_m(r,\tau)$ is the maximum

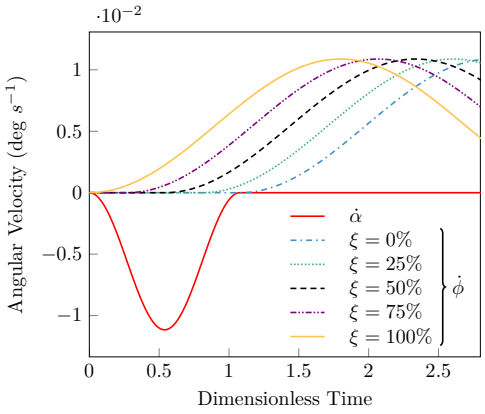

Figure 3: Sweeping and pitching velocities as a function of dimensionless time during the clap-and-peel. For 0% overlap during the peel phase, the wing completes the pitching motion before the sweeping begins. For 100% overlap, the wing begins to pitch and sweep simultaneously.

camber of the wing section as a function of spanwise position r and time τ, p is the non-dimensional chordwise position at which the maximum height of the local chord appears. The maximum ordinate of the mean line is assumed to be in the mid-chord position [12], i.e., $p = 0.5$. The instantaneous maximum camber $h_m(r, \tau)$ is expressed as

$$h_m(r,\tau) = \frac{h_m(r)}{\Delta\tau^*}\left(\tau - \tau^* - \frac{\Delta\tau^*}{2\pi}\sin\left[2\pi\left(\tau-\tau^*\right)/\Delta\tau^*\right]\right) \tag{5}$$

where $h_m(r)$ represents the maximum camber of the wing, which varies linearly from the wing's root to its tip and is defined as,

$$\frac{h_m(r)}{c(r)} = \left(\frac{h_{m,root}}{C_{r_2}} - \frac{h_{m,root}}{C_{r_2}}\frac{r}{R}\right) \tag{6}$$

where $h_{m,root}$ and $h_{m,tip}$ are the maximum height at the root and tip of the wing, respectively. C_{r_2} is the chord at the radius of the second moment of wing area (r_2). Figure. 2b shows the variation in the camber across different wing sections. An essential parameter, denoted as ξ, is introduced in this study, which determines the degree of overlap between pitching and sweeping motions. This parameter previously discussed in the two-dimensional work by Arora et al. [13] played an important role in the lift enhancement, and its contribution to the three-dimensional lift will be examined here. It is expressed here in % and dictates the timings of downstroke, flip, upstroke and clap. Figure 3 shows the angular velocities of pitching and sweeping as a function of dimensionless time at various degrees of overlap. The various kinematic parameters used in the study are listed in Table 1.

Figure 4 illustrates the schematics of wing kinematics at various time instants during one cycle, along with their corresponding wing and inertial coordinates. The trajectory of any arbitrary point on the wing($\mathbf{W}$) is described by orienting the wing with respect to the reference inertial frame $\mathbf{N}$, which is fixed to the stroke plane, using a (1–3) sequence of Euler angles, $\phi(\tau)$ and $\alpha(\tau)$.

$$\begin{Bmatrix} X^N \\ Y^N \\ Z^N \end{Bmatrix} = \begin{bmatrix} \cos(\phi) & -\cos(\alpha)\sin(\phi) & \sin(\alpha)\sin(\phi) \\ \sin(\phi) & \cos(\alpha)\cos(\phi) & -\cos(\phi)\sin(\alpha) \\ 0 & \sin(\alpha) & \cos(\alpha) \end{bmatrix} \begin{Bmatrix} X^W \\ Y^W \\ Z^W \end{Bmatrix} \tag{7}$$

Therefore, the lift C_L and drag C_D coefficients were calculated as follows:

$$C_L = \frac{2F_Z^N}{\rho S U^2} \tag{8}$$

$$C_D = \begin{cases} \frac{2\left(F_X^N\sin\phi - F_Y^N\cos\phi\right)}{\rho S U^2}, & \tau \le T/2 \\ \frac{2\left(-F_X^N\sin\phi + F_Y^N\cos\phi\right)}{\rho S U^2}, & \tau > T/2 \end{cases} \tag{9}$$

where F_X^N, F_Y^N and F_Z^N are the resultant forces in the inertial frame.

The Reynolds number is defined as $\mathrm{Re} = U\bar{c}/\nu$, where U is the reference velocity ($U = 2fr_2\phi_m$), ν

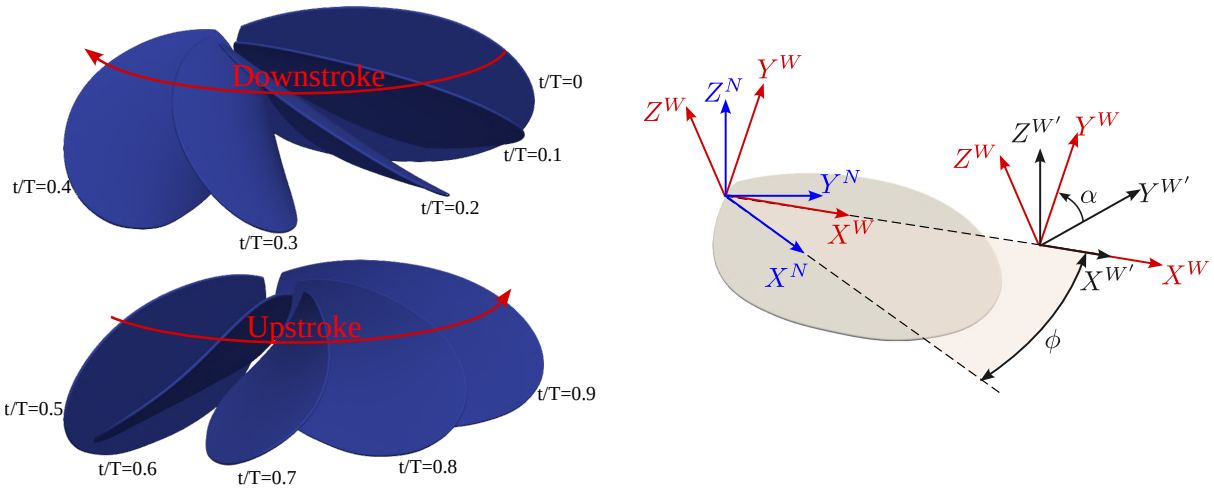

Figure 4: Schematics of wing kinematics during one stroke cycle.

is the kinematic viscosity, f is the wingbeat frequency, r_2 is the radius of second moment of wing area, and ϕ_m is the sweep amplitude. The fruit-fly exhibits a Reynolds number approximately in the order of ($\sim 10^2$). In the present study, we examine the aerodynamic forces and flow structures on the wing with a flapping frequency of approximately 200 Hz, operating at a Reynolds number of 200.

3 NUMERICAL METHODOLOGY

The present study involves the applicability of an in-house fluid solver based on the LBM [19, 14, 20, 15], which is used to analyze the flow behaviour around deforming wings performing clap-and-peel and to calculate the forces resulting from fluid-structure interaction.

3.1 Fluid solver

The density, velocity, and temperature fields in Navier-Stokes equation-based computational fluid dynamics (CFD) solvers are found by solving the governing equations of these variables, which include the conservation of mass, momentum, and energy. Conversely, the LBM solves a discretized version of the non-dimensionalized lattice Boltzmann equation (LBE) as a function of space ($\mathbf{x}$), time (t), and phase space ($\mathbf{e}_\alpha$). In this case, the particle distribution functions change at each time step due to streaming and collision processes [21].

The LBE includes a collision operator that simulates the effects of atomic or molecular collisions in a gas or liquid system. The Bhatnagar-Gross-Krook (BGK) or single relaxation time (SRT) model is the most popular model [22, 23, 24, 25]. However, the SRT model faces numerical instability at high Reynolds numbers, especially when using low relaxation time values. Furthermore, it often exhibits spurious oscillations in force measurements, as noted by [14]. A more robust multi-relaxation-time (MRT) model has been implemented to address these disadvantages [26]. Rather than relaxing particle distribution functions toward their equilibrium distribution functions, a transformation is performed into moment space. This method enables the independent relaxation of individual moments, allowing the relaxation rates of higher-order moments to be adjusted for improved stability. The proposed MRT approach addresses the limitations of the previous method (SRT) and provides more accurate and stable solutions for analyzing fluid flow. Additionally, a dynamic mesh refinement technique is used where a high-resolution grid region surrounds and moves with the wing. This approach significantly improves the accuracy of force measurements while being efficient in terms of computational resources. Further details about the fluid solver, mesh refinement, and validations can be found in [15].

3.2 Validation of a test case

In order to validate the solver for the simulation of deforming geometries, a case of a single rectangular wing performing flapping motion with time-varying camber and twist is simulated at Re=800. The plate with an aspect ratio (R/c) of 3.33 is placed at the centre of the flow domain, executing pitching and

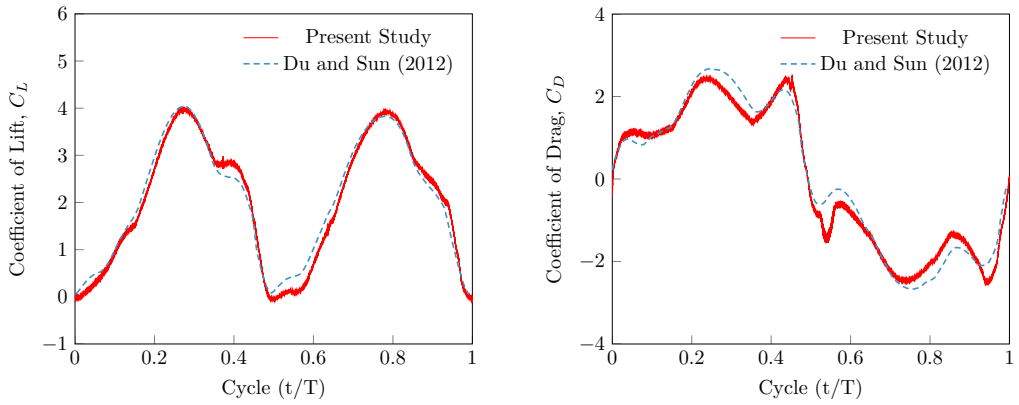

Figure 5: Time history of (a) lift and (b) drag coefficient compared with the results of Du and Sun [27] over one stroke cycle.

sweep (upstroke/downstroke) motion about its root. The axis of the pitching rotation is located at a quarter chord from the leading edge. The plate has a chord 100 lattice units with a thickness of 1% of the chord. The outflow boundary condition is enforced on all six faces of the fluid computational domain. The boundary was placed at a distance of $6 \times c$ from the centre in all six directions. The comparison of instantaneous lift and drag coefficients is shown in Fig. 5. The results obtained match well with the results of Du and Sun [27], indicating that the solver's ability to solve the deforming geometry problems accurately. The difference between these two estimations could be due to the unspecified boundary conditions in the literature and slight variations in the wing kinematics, which were digitized from images in the reference paper.

3.3 Computational Domain and Grid Convergence Test

In the current study, a computational domain measuring $10C \times 10C \times 10C$ (where C represents the chord length) was utilized for performing the clap-and-peel simulation. The domain was strategically positioned with wings at the centre. Outflow boundary condition was imposed on all six faces of the cubical domain. As mentioned earlier, a finely meshed conformal block is employed around the wings in order to enhance resolution and mitigate spurious force oscillations commonly encountered in LBM. This conformal block, measuring $3C \times 1.5C \times 3C$, moves synchronously with the wings and effectively ensures improved simulation accuracy and stability. Before conducting extensive numerical simulations, the test for grid convergence was performed for the case with the highest degree of overlap. The simulations were performed on four progressively refined spatial resolutions of $\Delta x = 0.0113C$, $\Delta x = 0.0075C$ and $\Delta x = 0.0065C$ to evaluate the influence of grid size on simulation results. It is important to mention that the forces generated by both wings are identical. Therefore, all subsequent references to instantaneous lift and drag coefficients represent values per unit wing. A comparison of instantaneous lift and drag coefficients with the mesh resolution is shown in Figure 6. Observations indicate that curves with refinements of $\Delta x = 0.0075C$ exhibit strong concordance. Consequently, a grid size of $\Delta x = 0.0075C$ is deemed adequately refined for the present study and has been utilized for all the simulations.

4 RESULTS AND DISCUSSION

In this section, results obtained from three-dimensional numerical simulation of flapping wings employing "clap-and-peel" motion using LBM are presented and discussed. The pitching and sweeping overlap (ξ) effect on the average lift and drag over a cycle is also discussed in detail. To examine the aerodynamic impacts of ξ, we have established multiple simulation scenarios with varying values of ξ (0%, 25%, 50%, 75%, and 100%). We first study the result obtained for the case with $\xi = 100\%$. Figure 7a presents the temporal behaviour of the instantaneous lift coefficient and the flow field at a specific point in the cycle. In addition, the corresponding drag coefficients are shown in Fig 7b. Furthermore, the impact of clap-and-peel between a pair of wings is compared to the behaviour of a single wing without any interaction between wings. All simulations are evaluated based on the findings from the second cycle

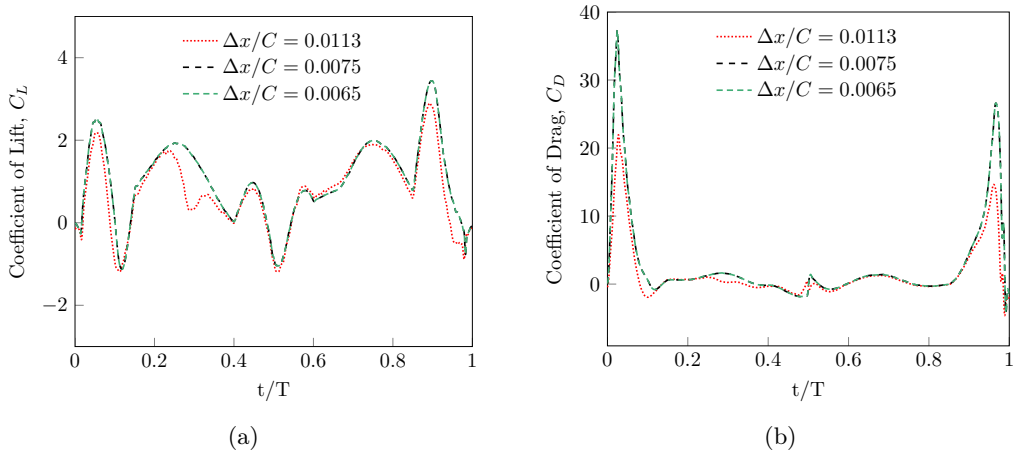

Figure 6: Effect of mesh size on the instantaneous (a) lift and (b) drag coefficients.

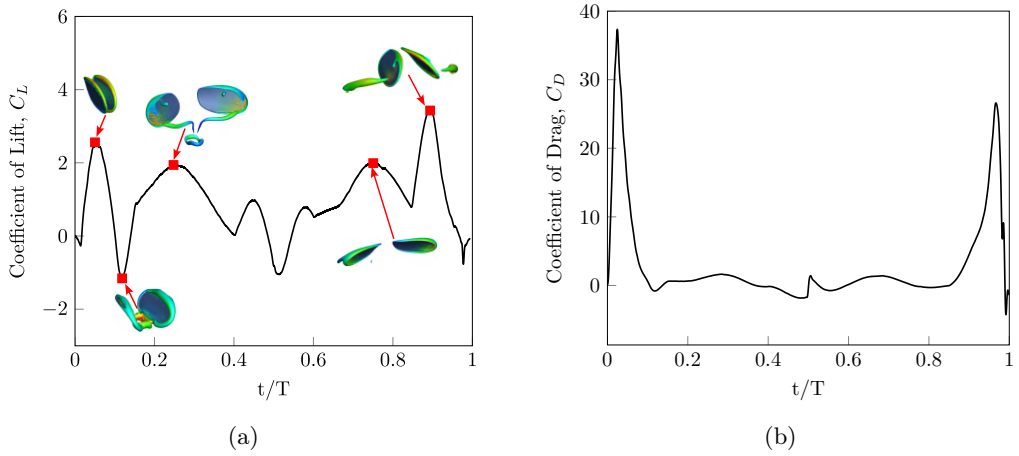

Figure 7: Time history of (a) lift coefficient and flow field (Qcriterion=5E-6) coloured with velocity magnitude (b) drag coefficient.

under all circumstances. Given the similarity between the forces and flows of the left and right wings, we will focus solely on discussing the left wing.

During the peel phase, the initial peak in the force coefficient is due to the wing's acceleration from a stationary position followed by a negative value of lift coefficient at the end of the phase. The positive peak in lift coefficient is observed due to the rapid formation of a strong vortex pair at the leading edge of the wings. The dip in force coefficients at the end of the peel phase is caused by the deceleration of the wings. As the angular velocity decreases, the wings experience a decrease in force coefficients due to the flow pushing on their upper surface.

Next, we examine the forces and flows in the successive period (t/T = 0.07-0.88), during which the wing executes the downstroke, flip, and upstroke. During this phase, the wing performs a sweeping motion consisting of the downstroke (t/T = 0.07-0.45), the flip (t/T = 0.45-0.49), and the upstroke (t/T = 0.49-0.88). Figure 8 shows the normalised spanwise vorticity ($\hat{\omega} = \omega \cdot C/U$) and velocity vectors at the pitching axis in a plane perpendicular to the stroke plane. The attached negative LEV grows as the downstroke progresses, and the lift coefficient reaches a local maximum around mid-stroke. At the end of the downstroke (t/T= 0.4-0.5), the wing flips to maintain a positive angle of attack during the upstroke. The acceleration of the wings' pitching causes the force coefficient to increase, followed by a decrease in the lift coefficient. This is due to the angular deceleration at the end of the flip phase. As the upstroke commences, the lift coefficient increases due to the wing's acceleration and the growth of the attached positive LEV. Observations indicate the presence of spanwise flow moving from the wing root to the wing tip, which helps to stabilise the LEV during downstroke and upstroke. The lift reaches a local maximum before declining as the wing decelerates. The upstroke is followed by the clap phase (t/T= 0.88 - 0.96), during which the wings execute a clapping motion around the leading edge. Significant peaks

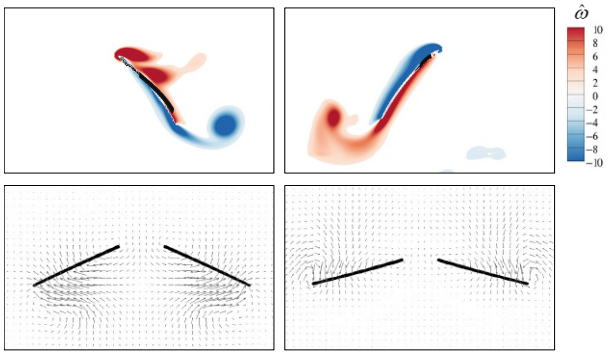

(a) t/T = 0.25 (b) t/T = 0.75

Figure 8: Normalised spanwise vorticity and velocity vectors at the pitching axis in plane normal to the stroke plane during (a) downstroke and (b) upstroke

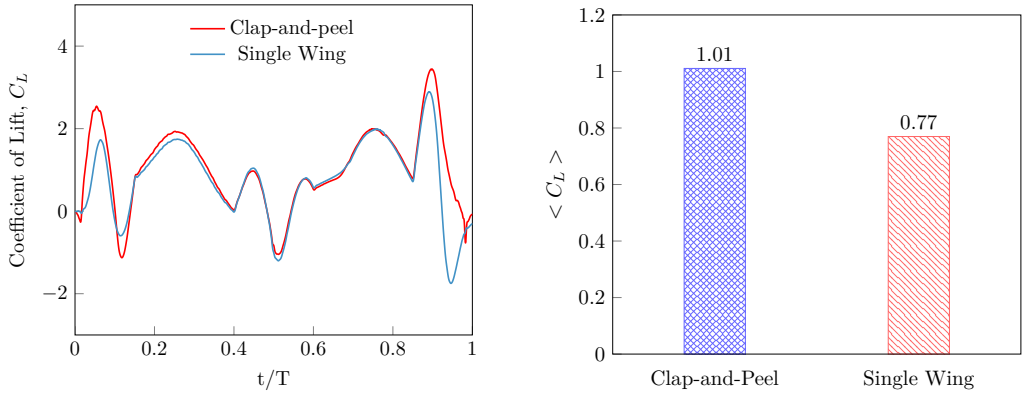

(a) (b)

Figure 9: (a) Instantaneous and (b) average lift coefficient compared with the single wing performing clap-and-peel kinematics.

were detected in both C_L and C_D, such as during the fling phase. This is due to the rapid formation of a strong vortex pair near the trailing edge, accompanied by the addition of downward jet momentum.

The flow of the single-wing performing the same kinematics has been computed, and the results are presented here subsequently. Figure 9a compares the time history of lift coefficients for one complete cycle. First, we compare the instantaneous lift and drag coefficient during the peel and clap phase; the peaks in force coefficient are lower compared to the pair of wings. This is due to the non-existence of wing-wing interaction for the single wing. As the cycle approaches its end ($t/T = 0.96 - 1.0$), a negative peak in C_L can be observed for the single wing. This can be explained by the wing's angular deceleration in the later portion of the clap, as well as by the associated flows on the wings forcing it downward. However, during the downstroke, flip and upstroke phases C_L remains the same. There is a slight difference in the peaks of C_L during the downstroke. This is due to the shed vortices from the peel phase aiding in the formation of stronger and more stable LEV during the downstroke.

Averaging C_L over one cycle gives the mean lift $< C_L >$ and drag coefficient $< C_D >$. The value of $< C_L >$ for the described flapping motion with clap-and-peel compared to the single wing performing the same kinematics is shown in Fig. 9b. The $< C_L >$ increased by 31.2% for the wing-pair compared to the single wing. This is caused by the wing-wing interaction, which creates resistance during the clap-and-peel phases, increasing the lift coefficient.

4.1 Effect of Overlap

In order to investigate the effect of overlap (ξ), we vary ξ during wing during wing pitching for peel, flip and clap phases. For the wing with $\xi = 0\%$, the wings come to rest at the end of the pitching motion, and then only the sweep starts. However, for the wings with a degree of overlap of 100%, the pitching and sweeping motion start simultaneously. Similarly, this corresponds to 25%, 50% and 75% overlap

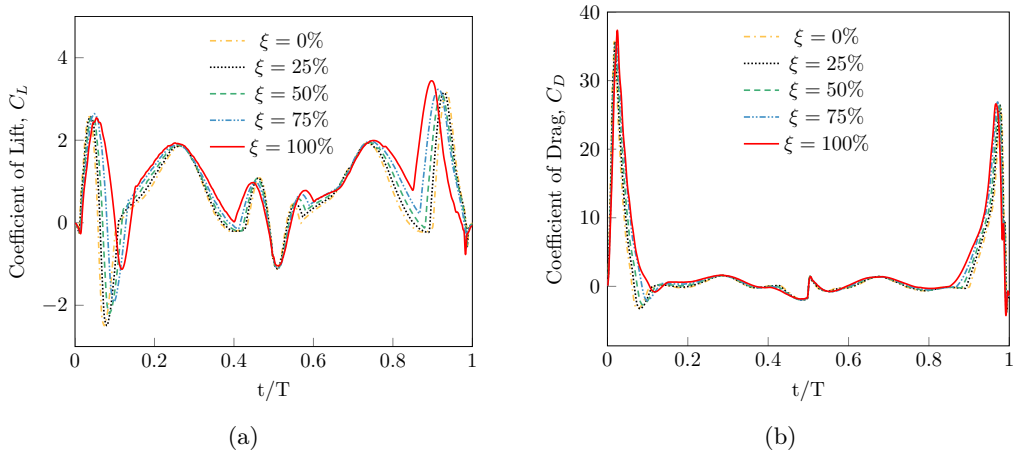

Figure 10: Time history of (a) lift and (b) drag coefficient for varying overlap parameter.

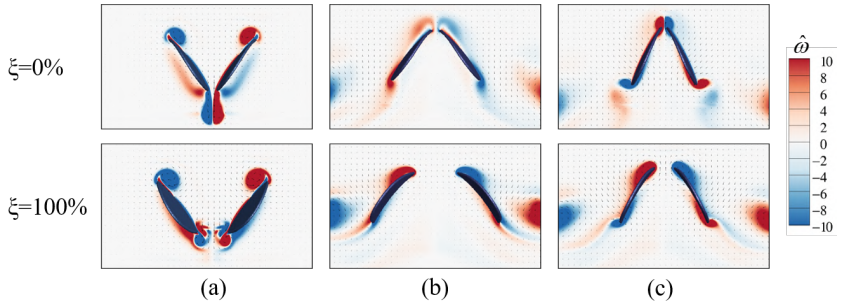

Figure 11: Normalised vorticity and velocity vector in a vertical plane at the middle of wing length at (a) end of peel phase, (b) start of clap phase and, (c) maximum lift during clap phase.

between pitching and sweeping. Time history of Lift and drag coefficients for the five cases (ξ =0%, 25%, 50%, 75%, and 100%) are shown in Fig. 10. For the peel phase, the first peak in force coefficient is similar for all the cases. However, a lower negative C_L at the end of the peel phase is observed for the case with a higher degree of ξ. Figure 11 shows the normalised vorticity and velocity vector in a vertical plane at the midpoint of the wing's length. It can be observed that the downward momentum of the flow generated during the peel phase impacts the wing's upper surface at 0% overlap. However, at $\xi = 100\%$, the downwash moves through the space between the wings as they sweep apart.

During the clap phase, the acceleration of the wing pitching occurs earlier during the clap phase when ξ has a greater value. Figure 11(b) and 11(c) shows the spanwise vorticity and velocity vector at the onset of the clap phase and at the point of maximum lift coefficient. The LEV from the end of the upstroke remains attached at higher degrees of overlap as the wing claps; however, it gets dissipated at $\xi = 0\%$ before the start of the clap phase. This corresponds to the initial increase in force coefficients, resulting in a higher peak C_L. During the downstroke, flip, and upstroke phases, the peaks in force coefficients are identical. However, the values of C_L and C_D remain consistently higher throughout the phase when ξ is higher. Figure 12 shows the normalized spanwise vorticity at various spanwise locations at the end of the peel phase. The shed vortices generated during the peel phase attach to the LEV generated during the downstroke for cases with a higher degree of overlap. These vortices increase C_L as the downstroke progresses. In contrast, for $\xi = 0\%$, the vortices dissipate before the downstroke begins.

To compare the average forces generated in each case, the lift and drag coefficients were averaged over a cycle, as shown in Fig. 13. The average lift $< C_L >$ and drag $< C_D >$ coefficient produced by the wing is higher as we increase the degree of overlap ξ. For the case with the highest value of ξ, the increase in $< C_L >$ is almost 36.4% higher as compared to the case with $\xi = 0\%$. Also, the average drag coefficient ($< C_D >$) produced in the $\xi = 100\%$ is higher than the corresponding lower ξ cases. However, the slope of increase in $< C_D >$ is larger from $\xi = 0$ to 50%, as compared to the rest of the cases.

(a) (b)

Figure 12: Normalized spanwise vorticity at the end of peel phase at location 0.2R, 0.5R and 0.8R from the wing root for (a) $\xi = 0\%$ and (b) 100%

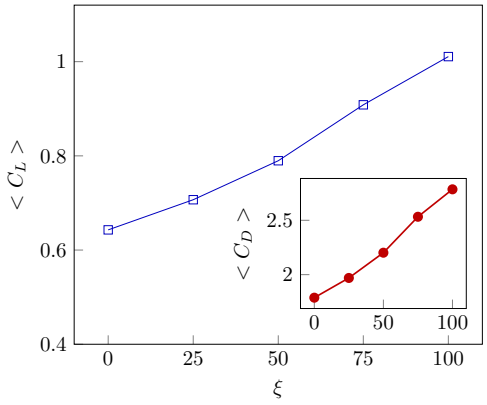

Figure 13: Mean lift and drag with varying overlap parameter.

5 CONCLUSION AND FUTURE WORK

The current study focuses on examining the aerodynamics of thrust generation and measuring the average lift and drag in the tiniest insects using the "clap-and-peel" motion. The kinematics of *Drosophila melanogaster* flight is determined by characteristics, including Reynolds number, pitching-sweeping overlap, sweep angle, angle of attack, wing separation, twist, camber, and others. For this purpose, we use an in-house numerical fluid solver that is based on the MRT version of LBM. This solver features a dynamic mesh refinement technique that enhances the resolution of the grid region surrounding the moving geometry. It is parallelized using OpenMP and can run on multiple cores with excellent scalability. The oscillations in force measurements that are frequently observed in LBM are eliminated by applying Grad's boundary condition to deformable boundary scenarios. The benchmark case of flapping rectangular wings with time-varying chordwise camber and twist was used to validate the solver's applicability for simulating moving and deforming boundary problems, resulting in outstanding agreement.

Numerical simulations of a three-dimensional wing planform of fruit-fly emulating "clap-and-peel" kinematics at different combinations of pitching-sweeping overlaps (ξ = 0%, 25%, 50%, 75% and 100%) at Re=200 are performed. It is found that the mean lift increases by 36.4% with increase in overlap. Upon further analysis of vortical structures, it is observed that a strong LEV is consistently present when ξ = 100%. This occurs because the shed vortices during the clap-and-peel phases are captured by the wings during the upstroke and downstroke, accumulating a stronger influx of fluid and resulting in higher net circulation compared to 0% overlap. Future work will focus on assessing the combined effect of variations in all the listed parameters and determining the optimal kinematics that minimise power consumption during flapping.

References

[1] Bor-Jang Tsai and Yu-Chun Fu. Design and aerodynamic analysis of a flapping-wing micro aerial vehicle. *Aerospace Science and Technology*, 13(7):383–392, 2009.

[2] Wei Shyy, Hikaru Aono, Chang-kwon Kang, and Hao Liu. *An introduction to flapping wing aerodynamics*, volume 37. Cambridge University Press, 2013.

[3] Laura A Miller and Charles S Peskin. Flexible clap and fling in tiny insect flight. *Journal of Experimental Biology*, 212(19):3076–3090, 2009.

[4] Fang-Bao Tian, Haoxiang Luo, Jialei Song, and Xi-Yun Lu. Force production and asymmetric deformation of a flexible flapping wing in forward flight. *Journal of Fluids and Structures*, 36:149–161, 2013.

[5] Mustafa Percin, Bas van Oudheusden, and Bart Remes. Flow structures around a flapping-wing micro air vehicle performing a clap-and-peel motion. *AIAA Journal*, 55(4):1251–1264, 2017.

[6] Charles Porter Ellington. The aerodynamics of hovering insect flight. iii. kinematics. *Philosophical Transactions of the Royal Society of London. B, Biological Sciences*, 305(1122):41–78, 1984.

[7] Charles Porter Ellington. The aerodynamics of hovering insect flight. iv. aerodynamic mechanisms. *Philosophical Transactions of the Royal Society of London. B, Biological Sciences*, 305(1122):79–113, 1984.

[8] Mark Jankauski, Ziwen Guo, and I.Y. Shen. The effect of structural deformation on flapping wing energetics. *Journal of Sound and Vibration*, 429:176–192, 2018.

[9] Fritz-Olaf Lehmann, Hao Wang, and Thomas Engels. Vortex trapping recaptures energy in flying fruit flies. *Scientific Reports*, 11(6992):2045–2322, 2021.

[10] A. Roland Ennos. The kinematics and aerodynamics of the free flight of some diptera. *Journal of Experimental Biology*, 142(1):49–85, 03 1989.

[11] Simon M. Walker, Adrian L. R. Thomas, and Graham K. Taylor. Deformable wing kinematics in free-flying hoverflies. *Journal of The Royal Society Interface*, 7(42):131–142, 2010.

[12] Gang Du and Mao Sun. Effects of unsteady deformation of flapping wing on its aerodynamic forces. *Applied Mathematics and Mechanics*, 29:731–743, 2008.

[13] Nipun Arora, Amit Gupta, Sanjeev Sanghi, Hikaru Aono, and Wei Shyy. Lift-drag and flow structures associated with the "clap and fling" motion. *Physics of Fluids*, 26(7):071906, 2014.

[14] Nipun Arora, Amit Gupta, and Wei Shyy. A shifting discontinuous-grid-block lattice boltzmann method for moving boundary simulations. *Computers & Fluids*, 125:59–70, 2016.

[15] Farhanuddin Ahmed, Amit Gupta, and Nipun Arora. An eulerian based geometry conforming grid-block dynamic mesh refinement for the lattice boltzmann method. *Physics of Fluids*, 35(10), 2023.

[16] Belkis Erzincanli and Mehmet Sahin. The numerical simulation of the wing kinematics effects on near wake topology and aerodynamic performance in hovering drosophila flight. *Computers & Fluids*, 122:90–110, 2015.

[17] Daniel Drevon, Sophie R. Fursa, and Allura L. Malcolm. Intercoder reliability and validity of webplotdigitizer in extracting graphed data. *Behavior Modification*, 41(2):323–339, 2017.

[18] Libéria Souza Torquato, Daniel Mattos, Bruna Palma Matta, and Blanche Christine Bitner-Mathé. Cellular basis of morphological variation and temperature-related plasticity in drosophila melanogaster strains with divergent wing shapes. *Genetica*, 142:495–505, 2014.

[19] Nipun Arora, Amit Gupta, Sanjeev Sanghi, Hikaru Aono, and Wei Shyy. Flow patterns and efficiency-power characteristics of a self-propelled, heaving rigid flat plate. *Journal of Fluids and Structures*, 66:517–542, 2016.

[20] Nipun Arora, Chang-kwon Kang, Wei Shyy, and Amit Gupta. Analysis of passive flexion in propelling a plunging plate using a torsion spring model. *Journal of Fluid Mechanics*, 857:562–604, 2018.

[21] Cyrus K. Aidun and Jonathan R. Clausen. Lattice-boltzmann method for complex flows. *Annual Review of Fluid Mechanics*, 42(Volume 42, 2010):439–472, 2010.

[22] Sauro Succi. *The Lattice Boltzmann Equation for Fluid Dynamics and Beyond*. Oxford University Press, New York, 2001.

[23] Renwei Mei, Dazhi Yu, Wei Shyy, and Li-Shi Luo. Force evaluation in the lattice boltzmann method involving curved geometry. *Phys. Rev. E*, 65:041203, Apr 2002.

[24] AA Mohamad. *Lattice boltzmann method*. Springer, London, 2011.

[25] Fabian Bosch, Shyam S. Chikatamarla, and Ilya V. Karlin. Entropic multirelaxation lattice boltzmann models for turbulent flows. *Phys. Rev. E*, 92:043309, Oct 2015.

[26] Timm Krüger, Halim Kusumaatmaja, Alexandr Kuzmin, Orest Shardt, Goncalo Silva, and Erlend Magnus Viggen. *Theory of the lattice Boltzmann method: From the Boltzmann equation to the lattice Boltzmann equation*. Springer International Publishing AG Switzerland, 2016.

[27] Gang Du and Mao Sun. Aerodynamic effects of corrugation and deformation in flapping wings of hovering hoverflies. *Journal of Theoretical Biology*, 300:19–28, 2012.